Pure Appl. Geophys. 172 (2015), 2247–2264

DOI 10.1007/s00024-013-0713-7

Pure and Applied Geophysics

A Comparison of Seismicity Characteristics and Fault Structure Between Stick–Slip Experiments and Nature

T. H. W. Goebel,[1] C. G. Sammis,[1] T. W. Becker,[1] G. Dresen,[2] and D. Schorlemmer[2]

Abstract—Fault zones contain structural complexity on all scales. This complexity influences fault mechanics including the dynamics of large earthquakes as well as the spatial and temporal distribution of small seismic events. Incomplete earthquake records, unknown stresses, and unresolved fault structures within the crust complicate a quantitative assessment of the parameters that control factors affecting seismicity. To better understand the relationship between fault structure and seismicity, we examined dynamic faulting under controlled conditions in the laboratory by creating saw-cut-guided natural fractures in cylindrical granite samples. The resulting rough surfaces were triaxially loaded to produce a sequence of stick–slip events. During these experiments, we monitored stress, strain, and seismic activity. After the experiments, fault structures were imaged in thin sections and using computer tomography. The laboratory fault zones showed many structural characteristics observed in upper crustal faults, including zones of localized slip embedded in a layer of fault gouge. Laboratory faults also exhibited a several millimeter wide damage zone with decreasing micro-crack density at larger distances from the fault axis. In addition to the structural similarities, we also observed many similarities between our observed distribution of acoustic emissions (AEs) and natural seismicity. The AEs followed the Gutenberg–Richter and Omori–Utsu relationships commonly used to describe natural seismicity. Moreover, we observed a connection between along-strike fault heterogeneity and variations of the Gutenberg–Richter *b* value. As suggested by natural seismicity studies, areas of low *b* value marked the nucleation points of large slip events and were located at large asperities within the fault zone that were revealed by post-experimental tomography scans. Our results emphasize the importance of stick–slip experiments for the study of fault mechanics. The direct correlation of acoustic activity with fault zone structure is a unique characteristic of our laboratory studies that has been impossible to observe in nature.

Key words: Stick–slip experiments, fault structure, acoustic emission statistics, *b*-Value, seismicityanalysis, fractal dimension, slip localization.

[1] University of Southern California, Los Angeles, CA, USA. E-mail: tgoebel@usc.edu
[2] German Research Centre for Geosciences, Potsdam, Germany.

1. Introduction

It is generally accepted that natural fault zones can only be partially described by planar, frictional interfaces, and should, instead, be regarded as complex zones of deformation. This complexity, with such inherent fault properties as frictional behavior, controls the mechanical response of faults when subjected to tectonic loading stresses. Recent results (Hori *et al.* 2004; Barbot *et al.* 2012; Noda and Lapusta 2013) have shown that the distribution of materials that favor unstable (velocity-weakening) over stable (velocity-strengthening) slip along faults strongly affects earthquake distributions and the overall slip behavior of a fault. In addition to rheological heterogeneity, earthquake ruptures and slip are also controlled by geometric heterogeneity within the fault zone.

On a larger scale, models that include fault-system-induced interactions of earthquakes can produce seismicity characteristics similar to regional observations and replicate observed statistical relationships, including aftershock clustering, of natural seismicity (Ward 2000; Rundle *et al.* 2004; Dieterich and Richards-Dinger 2010). Consequently, fault complexity is connected to internal fault properties (e.g. structural and rheological heterogeneity) and external processes (e.g. pore-pressure changes, stress changes induced by other earthquakes). This study focuses on a comparison between intrinsic fault zone properties in the laboratory and in nature, with special emphasis on structural similarities.

The structure of natural fault zones can conceptually be described by a fault core surrounded by a zone of distributed damage (Caine *et al.* 1996; Ben-Zion and Sammis 2003). A fault core contains a gouge layer, anastomosing principal and secondary zones of slip localization (Fig. 2a). The surrounding damage zone consists of joints, variably fractured rock, and subsidiary faults over a wide range of length scales (Chester and Logan 1986; Chester *et al*. 1993; Faulkner *et al*. 2003; Dor *et al*. 2006); this topic has been reviewed by Wibberley *et al*. (2008) and Faulkner *et al*. (2010). The structure of fault zones can vary substantially, with large dependence on protolith composition and fluid–rock interactions (Schulz and Evans 2000; Faulkner *et al*. 2003, 2008; Smith *et al*. 2013). This structural heterogeneity strongly affects seismic activity along faults. It has been suggested that micro-seismicity is connected to fault heterogeneity, and micro-seismicity has been used to map fault asperities (Malin *et al*. 1989; Wiemer and Wyss 1997; Schorlemmer and Wiemer 2005). Seismicity studies also provide details about changes in strain accumulation and fault properties at depth (Nadeau and McEvilly 1995; Nadeau and McEvilly 1999). Fault-normal seismicity profiles have been used to infer the width of the fault core and fault roughness, and progressive fault smoothing with larger displacements (Powers and Jordan 2010).

Many of these seismicity studies have used laboratory results to aid understanding of seismicity variations and their underlying mechanisms in nature (Main *et al*. 1989; Wyss and Wiemer 2000; Schorlemmer *et al*. 2005; Sobiesiak *et al*. 2007; Narteau *et al*. 2009). Laboratory studies reveal, for example, the effect of stress (Scholz 1968; Amitrano 2003) and compositional heterogeneity (Mogi 1962) on frequency–magnitude distributions (FMD) of micro-seismic events. In the laboratory, seismic energy is predominantly radiated in the form of high-frequency acoustic emissions (AEs) during micro-cracking and micro-slip. These AEs mark distinct prefailure stages before sample fracture that are connected to sample dilation and rupture nucleation (Lockner *et al*. 1991a, b). AEs are initially distributed throughout the sample and then start to localize when approaching the point of rupture nucleation and maximum stress (Lockner *et al*. 1991a, b). Before the point of peak stress and failure a general increase in AEs and a decrease in *b* value are observed (Main *et al*. 1989; Meredith *et al*. 1990; Zang *et al*. 1998); these are explained by the growth and coalescence of the pre-existing micro-crack population (Main *et al*. 1992). AE events during stick–slip motion on rough fracture surfaces can be used to identify points of fault branching and increased geometric complexity (Thompson *et al*. 2009). Furthermore, AEs document micro-processes before a stick–slip event (Weeks *et al*. 1978; Thompson *et al*. 2005; Goebel *et al*. 2012), which is commonly considered as a laboratory-analog for earthquakes (Brace and Byerlee 1966; Byerlee 1970).

In experiments, the occurrence of slip instability is controlled by material properties, loading conditions, and the machine stiffness which supplies elastic energy to a propagating rupture (Dietrich 1978; Lockner and Beeler 2002). Variations in machine stiffness (Lockner and Byerlee 1990) and fault roughness evolution (Voisin *et al*. 2007) can cause a transition between stable and unstable sliding. In nature, elastic energy is stored in the surrounding lithology of a fault. A slip instability occurs if a nucleating rupture patch reduces a fault segment's strength more quickly than the driving stress is reduced (Byerlee 1970; Dieterich 1979; Lockner and Beeler 2002).

This emphasizes some of the analogies between experiments and nature, and emphasizes the importance of a detailed description of slip instability in the laboratory. The nucleation of slip instability can be described as a function of changes in sliding velocity and interface properties which evolve over time. Marone (1998) and Scholz (1998) have written comprehensive reviews of laboratory derived rate-and-state friction laws and their role in earthquake mechanics. In the laboratory, the occurrence of a slip instability is sensitive to fault zone composition. Quartz-rich granite powders, for example, are characterized by velocity weakening which favors slip instability (Green and Marone 2002) whereas phyllosilicates are characterized by velocity strengthening which supports stable sliding (Moore and Lockner 2004; Moore and Rymer 2007; Faulkner *et al*. 2011).

Most previous laboratory studies investigated the sliding characteristics and frictional properties of planar material interfaces. This study focuses on the mechanical properties and structures of faults that develop from saw-cut-guided, natural fracture surfaces, thus providing the opportunity to study naturally created fault complexity. Furthermore, our experiments produced a series of stick–slip events under upper crustal stress conditions, thus enabling us to study the mechanical and seismic consequences of early stages of fault evolution. In the following discussion we emphasize observed similarities between laboratory experiments and nature. Initially, we reveal similarities in fault structure and off-fault damage production, which will be linked with observed AE statistics which show temporal and spatial clustering analogous to natural seismicity. Last, we consider fault evolutionary processes in the laboratory, which can be assessed by systematic changes in the spatial distribution of AEs.

2. Method

In this section we describe sample preparation, loading conditions, and AE data analysis. More detailed treatment of the AE-acquisition system and experimental setup can be found in Stanchits *et al.* (2006) and Goebel *et al.* (2012, 2013), respectively. We report four experiments performed on cylindrical (radius = 40 mm, height = 107 mm) Westerly granite specimens at the German Research Centre for Geosciences (GFZ). The grain size of Westerly granite samples varies between 0.05 and 2.2 mm, with an average grain size of 0.75 mm (Stesky, 1978).

The experiments were conducted at room temperature and room-dry conditions. To accurately monitor elastic and inelastic sample deformation, AE sensors and strain gauges were glued directly to a specimen's surface. We designed the experiments so that most of the macro and micro-fracture activity was focused within the central region of each specimen away from the sample boundaries. This was accomplished by introducing saw-cut notches of different lengths (1.5–2.3 cm) at a 30° angle to the loading axis before the experiments. To minimize bending and to avoid rubber jacket damage at high confining pressures, we inserted 1 mm thick teflon sheets into the saw-cut notches which were of approximately equal widths. An overview of loading conditions can be found in Table 1 and the sample geometry is depicted schematically in Fig. 1a. The experiments were conducted under triaxial loading conditions at constant confining pressures ($\sigma_{xx} = \sigma_{yy}$). Vertical displacement rates were held constant at $\dot{\epsilon} \approx 3 \times 10^{-6}\,\mathrm{s}^{-1}$. The laboratory fault zones were created by initial, saw-cut-guided fracture followed by fault locking as a result of pressure increase (from P_c = 75 to 150 MPa), and, last, fault reactivation in the form of stick–slip motion (Goebel *et al.* 2012).

In contrast with an idealized model of stick–slip motion with linear stress increase and constant failure stresses, we observed a range of complexities in the stress curves of our tests (Fig. 1b). The stress increase before failure was characterized by large amounts of inelastic deformation. At the same time, we observed small, abrupt stress drops possibly because of local failure events and variations in both peak and residual stress after slip. Figure 1b shows differential stress and strain during the reloading of a previously faulted sample that led to the creation of six stick–slip events with large stress drops (LSD events) some of which

Table 1

Loading conditions and mechanical data for the four experiments presented

Sample	l_n (cm)	l_{RS} (MPa)	$P_{c_{frac}}$ (MPa)	$P_{c_{slide}}$ (MPa)	$\sigma_{max_{frac}}$ (MPa)	$\sigma_{max_{slide}}$ (mm)	$U_{x_{max}}$
WGRN04	1.5 ± 0.7	5.0 ± 0.15	75 ± 0.5	150 ± 0.5	635 ± 6	400 ± 6	3.0 ± 0.003
WGRN05	1.9 ± 0.7	4.2 ± 0.15	75 ± 0.5	150 ± 0.5	510 ± 6	296 ± 6	4.1 ± 0.003
WGRN07	2.2 ± 0.7	3.7 ± 0.15	75 ± 0.5	150 ± 0.5	450 ± 6	293 ± 6	4.3 ± 0.003
WGRN08	2.5 ± 0.7	3.0 ± 0.15	75 ± 0.5	150 ± 0.5	380 ± 6	288 ± 6	3.7 ± 0.003

The lengths of the saw-cut notches were gradually increased from WGRN04 to WGRN08 which led to a net reduction of rough surface area

l_n notch length, l_{RS} approximate length of the rough fracture surface, $P_{c_{frac}}$ confining pressure during fracture stage, $P_{c_{slide}}$ confining pressure during frictional sliding of the previously generated fault, $\sigma_{max_{frac}}$ maximum differential stress during fracture stage, $\Delta\sigma_{max}$ maximum differential stress during sliding, and $U_{x_{max}}$ maximum vertical displacement of loading piston

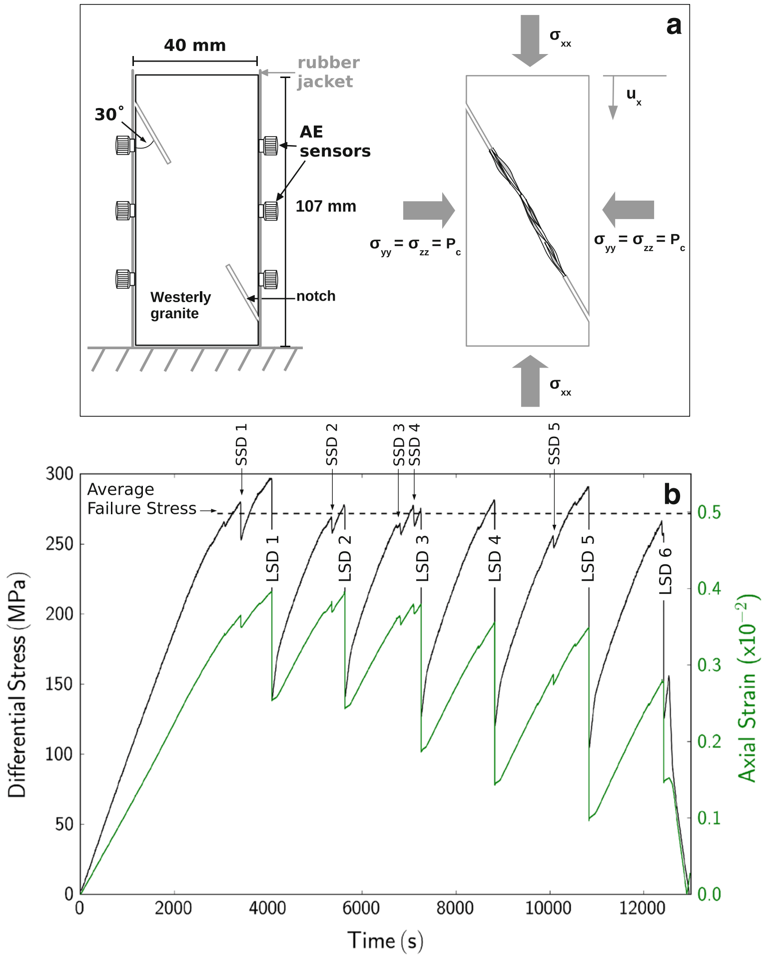

Figure 1
a Sample geometry and loading conditions of the triaxial tests. **b** Variations in stress and strain with small stress drop (SSD) and large stress drop (LSD) events during six stick–slip cycles

were preceded by smaller stress drop (SSD) events. The alternation of gradual stress increase and abrupt release of the stored elastic energy during slip is typical of all experiments.

2.1. Acoustic Emission Recordings and Magnitude Determination

To monitor seismically active deformation during stick–slip, we used a 16 channel seismic array of piezo-electric transducers with a resonance frequency at 2 MHz. We recorded full seismic waveforms at 10 MHz sampling frequency corresponding to a time resolution of 0.1 µs. The amplitude resolution was 16 bits. AE hypocenter locations were determined from first arrival times and active velocity measurements using transducers as ultrasonic-pulse senders. The location uncertainty was estimated at 1–4 mm, depending on the proximity of an event to the edge of the array.

The average amplitudes of the recorded AE events were computed from the maximum amplitudes at each channel in volts and corrected for geometric spreading between source and receiver.

On the basis of the corrected, averaged amplitudes (A), we assigned magnitudes:

$$M = \log_{10}\left(\frac{A}{A_c}\right) \tag{1}$$

where A_c describes a reference value.

2.2. *Statistical Analysis of Acoustic Emission Data*

In this section we describe the details of the statistical description of AE distributions in space and time, and of the FMD. The latter can be characterized by a power-law with an exponent (b value) that describes the relative proportion of small vs. large magnitude events (Ishimoto and Iida 1939; Gutenberg and Richter 1944):

$$\log N = a - bM, \quad (2)$$

where N is the number of AE events of magnitude larger than or equal to M and a is a constant representing the seismic activity. For a reliable estimation of b values, we required AE distributions to contain at least 150 events. b values were computed by use of the maximum-likelihood estimator (Aki 1965; Utsu *et al*. 1965; Bender 1983):

$$b = \frac{1}{\overline{M} - M_c}\log_{10}(\mathrm{e}). \quad (3)$$

Here, $\overline{M}$ is the mean magnitude, $\mathrm{e} = \exp(1)$ and M_c is the magnitude of completeness corrected for bin size to account for possible biases of discrete magnitude bin sizes (Utsu *et al*. 1965; Guo and Ogata 1997). We estimated M_c by inspection of large sets of FMDs and determined the deviation from the linearity of the cumulative histograms. We used a constant value for M_c assuming no significant changes in completeness. This is supported by stable array sensitivity and consistent, high-quality seismic records throughout the experiments. The total number of successfully located AE events for each experiment varied between 34,141 and 97,847, with relative magnitudes ranging from 0.84 to 5.0. While the minimum magnitude was likely related to the smallest detectable crack size, the maximum magnitude was limited by the analog input range of the digitizing cards. On the basis of the large AE data sets, we computed spatial variations in b value within the fault zone. To this end, we used the N nearest events to each point within a homogeneous 2D grid (0.1 mm grid spacing) that was located within the best-fit fault plane. Computing b values on the basis of a nearest neighbor approach ensures the same statistical significance and similar uncertainties at each grid point, while also increasing the spatial resolution, especially in areas of high AE density (details of spatial b value mapping and different methods are given by Wiemer and Wyss 2002). b Values were only computed for grid nodes that had sufficient AE events ($N > 150$) within a spherical volume with maximum radius of 5 mm. N was then varied between 150 and 600 events to test the stability of spatial b value patterns.

To describe aftershock rates after LSD events we used the Omori–Utsu relationship:

$$\frac{\mathrm{d}N}{\mathrm{d}t} = \frac{K}{(c+t)^p} \quad (4)$$

where $\mathrm{d}N/\mathrm{d}t$ is the aftershock rate and t is the time after slip. K, c and p are empirical fitting parameters. K is generally related to the productivity of an aftershock sequence, and it has been suggested it depends on mainshock magnitude (Utsu *et al*. 1965). c describes the length of the time window of initial deviation from a power-law decay and is typically small, ranging from $\lesssim 1$ day (Ogata 1999) down to values close to 0 (Reasenberg and Jones 1989; Shcherbakov *et al*. 2004; Narteau *et al*. 2009). These values can be affected both by catalog incompleteness immediately after a mainshock and by the mechanics of the faulting process, e.g., the stress level on a fault (Narteau *et al*. 2009). p is the rate decay exponent which is usually close to 1, and can vary between 0.5 and 1.9, especially during spatial mapping of aftershock data (Ogata 1999; Wiemer and Katsumata 1999). To estimate the empirical fitting parameters for aftershocks within the time interval $[t_a, t_b]$, we maximized the likelihood function suggested by Ogata (1999):

$$\log L(K, c, p; t_a, t_b) = N \log K - p\sum_{i=1}^{N}\log(t_i + c) - K\Lambda(c, p, t_a, t_b), \quad (5)$$

where

$$\Lambda(c,p,t_a,t_b) = \begin{cases} \log(t_b + c) - \log(t_a + c), & \text{for } p = 1 \\ \left((t_b + c)^{1-p} - (t_a + c)^{1-p}\right)/(1-p), & \text{for } p \neq 1 \end{cases} \quad (6)$$

To find the parameters that maximize this function, we used a simplex optimization algorithm, and investigated the parameter space to ensure the robustness of the maxima. The uncertainties in the parameters were estimated by bootstrap re-sampling. A performance test of the fitting algorithm can be obtained from a Kolmogorov–Smirnov test (KS test) that compares modeled and observed AE aftershock times (Woessner *et al*. 2004). The KS-test indicates if modeled and observed data originated from the same distribution. High values indicate that the Omori–Utsu relationship is a valid model for description of the observed aftershock rates.

To assess variations in the spatial distribution of AE events we computed the fractal dimension for events within individual interslip periods. To achieve this, we estimated sample densities on different scales by use of the pair correlation function (Feder 1988; Schroeder 1991), and determined the number of AE events within spherical volumes with increasing radii r_i:

$$\mu(R < r_i) = A_H r_i^{D_H} \tag{7}$$

where R is the distance vector between the current sample and all other AE events, μ is the AE density, A_H is a prefactor, and D_H is the fractal dimension, computed from the linear part of the power-law distribution of μ and r (Wyss *et al*. 2004). The radius r was logarithmically binned so that its values appear equally spaced in log space. As a result, less weight is given to data at large distances, adding to the robustness of the least-square estimates of fractal dimensions. The pair correlation function is analogous with the correlation integral (Grassberger 1983) used to estimate fractal dimensions of hypocenter locations in nature (Hirata 1989). We tested a range of different values for AE sample sizes, concluding that results were stable for more than 1,000–3,000 events, depending on AE catalog size. Uncertainties in D_H were estimated by bootstrap re-sampling and the reliability of fractal dimension estimates was tested by using known fractal geometries, i.e. the Sierpinski gasket (Schroeder 1991).

3. Results

3.1. Post-Experiment Fault Structure

To examine parallels between laboratory experiments and natural faulting, we monitored fault development starting from an incipient fracture surface. After completion of the experiments, we analyzed micro-structures on the basis of fault parallel and orthogonal thin sections of multiple specimens. Before this analysis, specimens were confined by the initial rubber tubing and additional steel clamps to preserve the post-experiment configuration of the sample as much as possible. Small movements along the fault were unavoidable, because of elastic rebound of the samples and rubber jackets after pressure removal, so offsets and crack widths in thin sections and CT scans deviated slightly (<1 mm) from those under in-situ conditions. To avoid further movement, specimens were impregnated with low-viscosity, colored (blue) epoxy-resin, immediately after the experiments. Use of the blue epoxy enabled clear distinction between connected pore space and sample mineralogy.

Figure 2b, c shows photographic images of a laboratory-created and a natural fault zone. The latter is a normal fault with pronounced zones of localized slip and a core deformation zone containing highly fractured material, gouge, and Riedel shears. This fault is located in South East Spain within the Almera Province (between Huercal Overa and Velez Rubio) and is part of the Alpujarride Complex. (Meijninger and Vissers (2006, 2007) give details about regional tectonics, lithology, and fault development.) In the laboratory, sample fracture and successive stick–slip events resulted in damage creation that also led to the formation of distinguishable structural features. The center of the laboratory faults were usually marked by a gouge layer containing larger clasts and localized zones of fine-grain material (Fig. 2c). The clasts have large size variations (from $\sim$5 to 500 μm) because of different stages of grain comminution and spatial-heterogeneous strain accumulation within the fault zone. By analogy with models of natural faults, we sub-divided our laboratory fault structures into three major zones:

1. A fault core with a width that varied between 0.3 and 1 mm containing clasts of different grain size and several zones of localized slip with very fine-grained material (>20 μm). The fault core shows evidence of shear deformation in form of zones of localized slip and Riedel shears within the core's gouge layer.

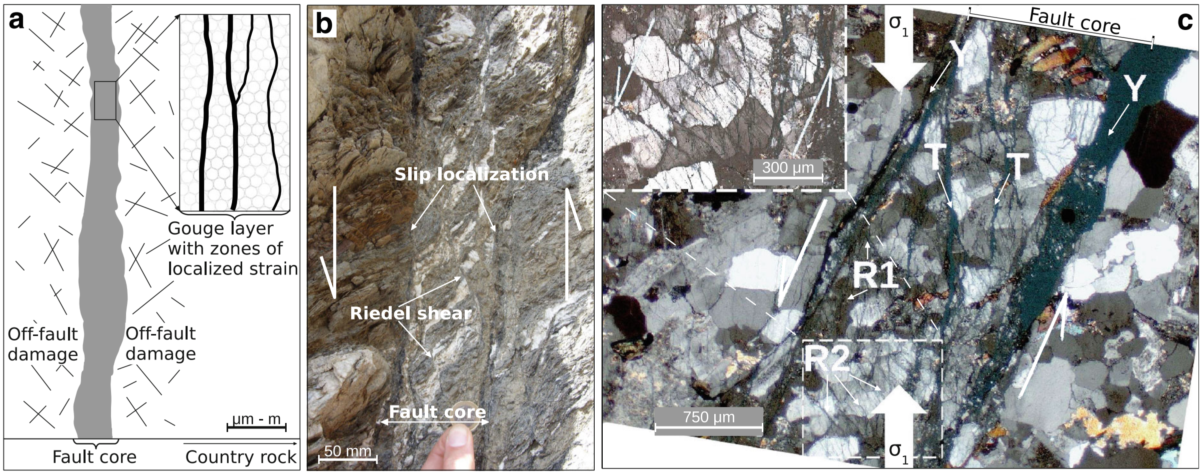

Figure 2

Comparison of natural and laboratory fault structures. **a** Schematic diagram of natural fault structure. **b** Photographic image of a natural fault zone that contains a gouge layer, zones of localized slip, and Riedel shears within the gouge layer. **c** Microscopic image of post-experiment thin section of a laboratory fault zone. The fault contains a gouge zone, off-fault damage, Riedel shears (R_1 and R_2; *inset*), principal slip zones (Y), and tensional cracks (T) sub-parallel to the direction of maximum stress

2. At larger distance from the fault axis, we observed a zone of enhanced damage and micro-cracking. This damage zone was characterized by grain boundary cracks, intergranular and transgranular cracks, and removal of grains from the edge of the damage zone which were subsequently assimilated into the gouge layer. Many of the larger flaws within the fault core and transitional damage zone had a preferred, low-angle (<30°) orientation relative to the fault axis. These cracks had extensional and shear components, similar to the observations for Riedel shears (Fig. 2b) and joints in nature.
3. The gouge layer and damage zone were embedded in the country rock which seemed largely undamaged within the thin sections.

We analyzed the density of micro-cracks at increasing distances from the fault axis (Fig. 3), identified by the blue-colored epoxy resin. For micro-crack density analysis, we removed all loose gouge particles from the fault surface to enable clearer distinction between gouge and transitional damage layer. The thin section in Fig. 3a depicts the damage micro-structure in a plane perpendicular to the fault plane (inset in Fig. 3a). The normalized crack density was computed as a function of distance between the interface of the fault core and the micro-crack damage zone by taking the ratio of intact to fractured material. The micro-crack damage is apparent from the black lines in Fig. 3a. The x axes are the same in Fig. 3a, b. The resulting density profile was smoothed by use of a 15-sample moving average filter. Micro-crack densities were generally highest close to the fault core and decreased with large fault normal distances. This suggests that most of the damage is caused by deformation processes within or at the edge of the fault core, and that these processes result in pervasive damage creation even at distances of several millimeters. In addition to the fault core-related damage zone, we observed secondary zones of increased crack density around larger flaws within the transitional damage zone (Fig. 3a). Thin sections from areas at large distances (>1.7 mm) from the gouge–damage zone interface contained little or no visible damage. We also determined the approximate extent of the damage zone from the distribution of the number of AE events relative to the fault core. To achieve this we projected the AE hypocenters into a best-fitting fault coordinate system and computed the number of AEs as a function of fault-normal distance (Fig. 3c). The AE activity was largest close to the fault axis and decreased with larger distances extending out to ~ 14 mm. For comparison, the AE density profile also shows the extent of fault core and micro-crack damage

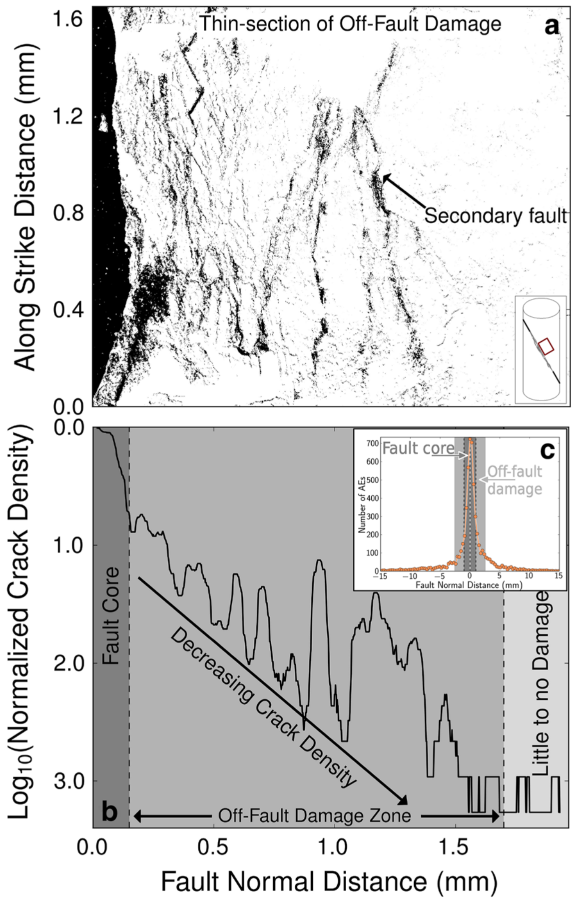

Figure 3

Micro-crack density distribution as function of fault normal distance. **a** Cracks and pore-space within a thin section of a typical, fault-adjacent region. The fault gouge was removed. The *inset* in **a** shows the location of the thin section (*red rectangle*) relative to the fault zone. **b** Crack density at increasing fault normal distance and fault structural units (i.e. fault core, off-fault damage zone, country rock with little damage). **c** Across-fault profile of AE activity for all AE events within a typical interslip period. The AE activity was binned every 0.3 mm

zones observed in thin-section images. This comparison revealed that the region of high AE activity extends out to further fault-normal distances than the micro-crack densities in thin sections, suggesting different resolution of the two methods, which is in agreement with earlier studies (Zang *et al.* 2000).

3.2. AE Distributions in Time and Space

In this section we discuss the connection between in-situ recordings of AE events and post-experiment fault structures. In addition to micro-structural analysis of thin sections we examined the structure of faults in post-experiment X-ray computer tomography (CT) scans. CT scans, which image density contrasts between pore space and the rock matrix, reveal a range of deformation-induced features. These features include preferred zones of slip, revealed as black linear zones and high AE activity in Fig. 4, and anastomosing, secondary cracks within a broader damage zone. The previously observed gouge layer is not clearly identifiable. However, we can determine the width of the fault damage zone outlined by the anastomosing crack network. This width varies between 1.5 and 4.5 mm, similarly to observations for thin sections. The thinnest part of the damage zone is located close to the center of the specimen at Y = 25–30 mm and Z = 42–47 mm in Fig. 4. AE hypocenter locations, which are usually guided by the fault orientation, cluster within this area. These AE clusters had relatively larger magnitudes at higher stresses closer to failure. The nucleation point of subsequent LSD event is located within this area in immediate proximity to a cluster of large-magnitude events. This reveals the close connection between fault structure and AE activity during loading and stress increase on our laboratory faults. Thin parts of the fault zone seem to locally intensify loading stresses, which would explain the relatively large AE activity and event magnitudes in this area, as discussed by Goebel *et al.* (2012).

In addition to the spatial variations of AE activity, we also observed systematic temporal changes in AE rates associated with LSD events. Numbers of AE events were comparably low before, and had a sharp peak at the onset of LSD events which was followed by a gradual decrease over several seconds (Fig. 5). The onset of LSD events was also connected to large-amplitude AE waveforms, which led to a $\sim$5 ms long saturation of the recording system. Although these waveforms appeared mostly clipped, their first-arrival times enabled accurate determination of slip onset times and locations of slip nucleation patches. After $\sim$5–10 ms, individual AE events could again be recorded and located. The AE activity decayed with time after the LSD onsets and reached the pre-failure level within $\sim$10–20 s. These AE events will be called aftershocks in the following discussion.

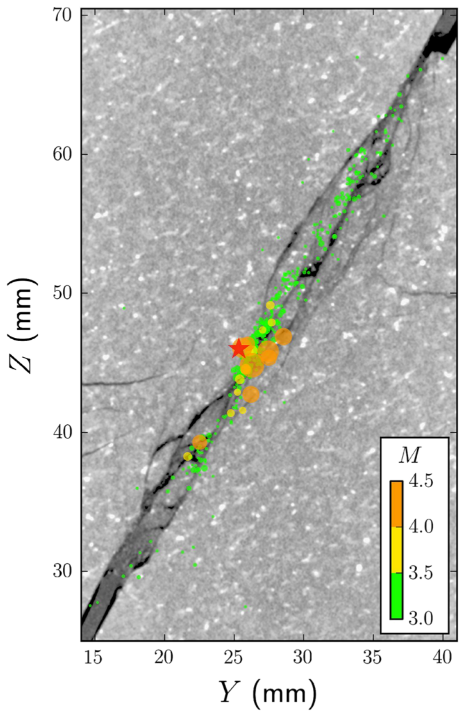

Figure 4
AE hypocenter distribution and magnitudes (*colored dots*) superimposed on a post-experiment CT scan image that shows fault structure and width. The displayed crack network is a result of the cumulative damage creation during sample fracture and six successive stick–slip events whereas the AE events shown occurred within a ∼15 min period leading up to an LSD event. The AEs occurred within a 5-mm slice centered at the CT image position. The *red star* shows the nucleation point of the LSD event (modified from Goebel *et al.* 2012)

AE aftershock rates decayed rapidly within the first few seconds after the LSD events and then more gradually over the next ∼20 s. This behavior can be described by the Omori–Utsu relationship. Our analysis revealed that the parameters of the Omori–Utsu relationship are very sensitive to the beginning of an aftershock period, whereas the end of the aftershock interval changed the results only marginally. We usually obtained the most stable results by setting the beginning of an aftershock sequence to the LSD onset times and the end to 30 s after slip onset. To exemplify the quality of aftershock fitting and the analogy with natural aftershock sequences, we plotted cumulative aftershock rates of a typical LSD event and aftershock rates of the M = 6.0, 2004 Parkfield event (Fig. 6, inset). Both events had relatively high KS statistics (p values = 0.5 and 0.9) showing that the Omori–Utsu relationship is a valid model for description of both data sets. Aftershock sequences during our experiments were limited to faults that developed from incipient fracture surfaces and were not observed during experiments on saw-cut surfaces. This emphasizes the importance of fault structural heterogeneity for temporal clustering of AE events.

Besides the generally observed Omori–Utsu aftershock decay, we were also interested in a comparison of FMD in the laboratory and in nature. Figure 7 depicts an example of a typical FMD of AE events that occurred within an interslip period. The FMDs usually have characteristics similar to those of Gutenberg–Richter type FMDs, with a pronounced power-law fall-off over more than one order of magnitude. The extent of the power-law decay is seen in both the approximately straight part of the FMD in log–log space and the stability of b values within this range of magnitudes (Fig. 7, inset).

We investigated spatial variations in b values within the interslip periods of LSD events. Spatial b value maps were characterized by localized regions of low b (Fig. 8b). Although these regions varied in size and shape, the centroid position remained largely stable over many successive stick–slip events. This result was independent of the number of AE events used for b value computations, even when the number of AEs was varied between 150 and 600 (Goebel *et al.* 2012). Low-b-value regions usually coincided with or were adjacent to regions of high seismic moment release (Fig. 8c), suggesting that the occurrence of large-AE events were of substantial importance in creating low-b-value regions. We compared FMDs within a low b value area and a "typical" fault region (Fig. 8b inset). The "typical" fault region was associated with a much smaller number of large-magnitude AE events ($M > 3.0$). Events with $M = 4.0$–4.9 were missing entirely during that period, which provides an explanation for the large differences in b values.

Our observations agree in several respects with spatial b value maps of the Parkfield section of the San Andreas fault (Fig. 8a). Both maps depict regions of anomalously low b value within a broader region of higher b values. In both cases, the difference between low and high b value regions is ∼0.4–0.5,

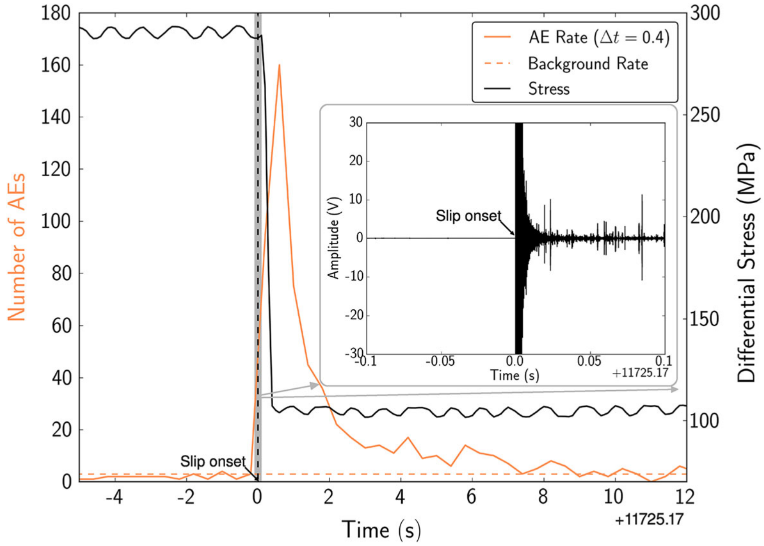

Figure 5
"Mainshock" identification on the basis of AE rate peaks and waveform recordings (*inset*). AE rates, computed for time bins of $\Delta t = 0.4$ (*orange line*), increase sharply at the time of slip whereas stress (*black*, *solid line*) drops abruptly. The apparent shift between the onset of stress drop and peak AE rate is caused by time binning and the saturation of the recording system immediately after slip. After the onset of slip, AE rates decreased gradually reaching the pre-failure rate at $\sim$10 s

and the regions of low *b* value mark the likely areas of future, large seismic events. The total range of *b* value variation is generally slightly larger in our experiments (0.7–2) than in nature (0.5–1.3). This shows that direct comparison of absolute *b* values is not possible. Differences between *b* values are likely to be because of different types of recording system, in the same way as between different seismicity catalogs and the corresponding magnitude scales. Nevertheless, relative variations in *b* value may be an expression of similar underlying micro-processes in nature and laboratory experiments.

3.3. Fractal Dimensions of AE Events

Whereas fault structures can be assessed only directly after completion of an experiment, for example, by using CT images and thin sections, AE events provide information about in-situ deformation and can thus be used to monitor changes in fault structure. We investigated the tendency of AEs to localize close to the fault plane to assess changes in the spatial extent of micro-cracking with each successive stick–slip event. To this end, we computed the fractal dimensions of AE hypocenter distributions (D_H) for each interslip period. In general, fractal dimensions of seismic events can vary between approximately 1 and 3. Strongly localized event clusters can drop below values of $D_H = 1$ (depending on observational scales), linear clusters have fractal dimensions slightly greater than 1, and event clusters that occur along a plane have $D_H \gtrsim$ values of 2 (Mandelbrot 1982). On the basis of these considerations, we expect volume-filling distributions of AEs to have fractal dimensions substantially larger than 2 which decrease when AEs start to occur predominantly along the fault surface. In practice, decreasing fractal dimensions can be connected to both localization at a surface and hypocentral clustering at points within the surface.

We conducted three control experiments on planar, saw-cut surfaces with specific roughness created by surface grinding with silicon carbide powder (Fig. 9). These experiments revealed AE distributions with fractal dimensions below 2 in all cases, thus the AE populations did not fill the entire fault plane. The smooth surface had a lower fractal dimension ($D_H = 1.48$) than the rough surfaces ($D_H = 1.79$–1.82). Following the observed connection between D_H and fault roughness, we analyzed variations in D_H with successive LSD events.

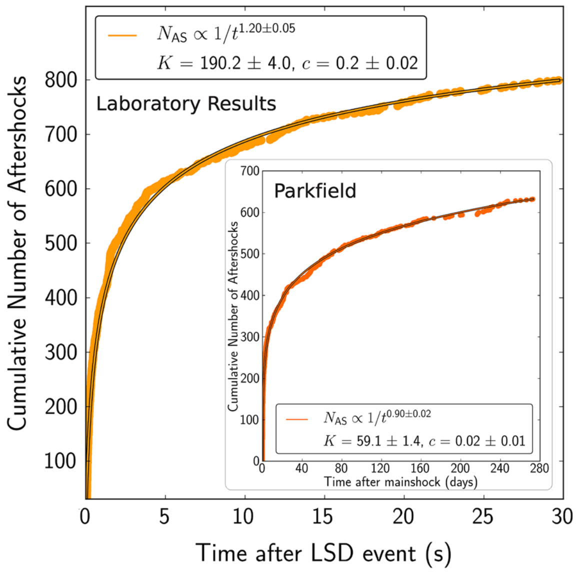

Figure 6

AE aftershocks decay as a power-law with time from the LSD event. This could be described by the Omori–Utsu relationship. The *orange markers* represent a typical, cumulative aftershock rate 30 s after an LSD event, and the *orange curve* shows the corresponding fit. The *inset* shows the cumulative aftershock rate and Omori–Utsu fit in a 280 day period after the M = 6.0, 2004 Parkfield event

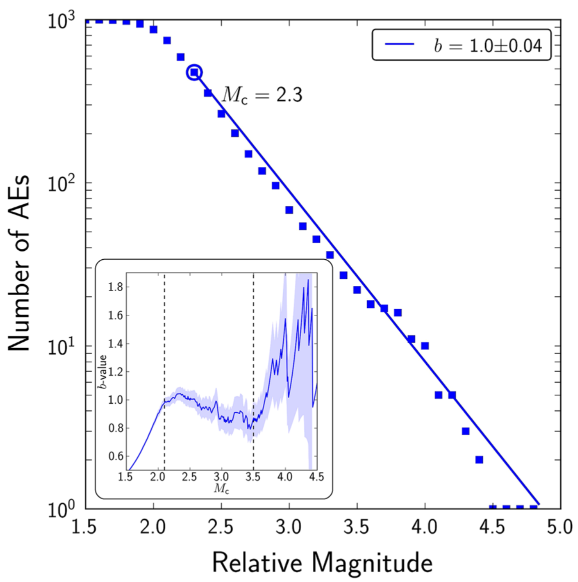

Figure 7

Frequency–size distributions of AEs in laboratory stick–slip experiments can be described by a power-law similar to the Gutenberg–Richter relationship with a slope b = 1 ± 0.04. This power-law spans ∼1.2 orders of magnitude (*inset*)

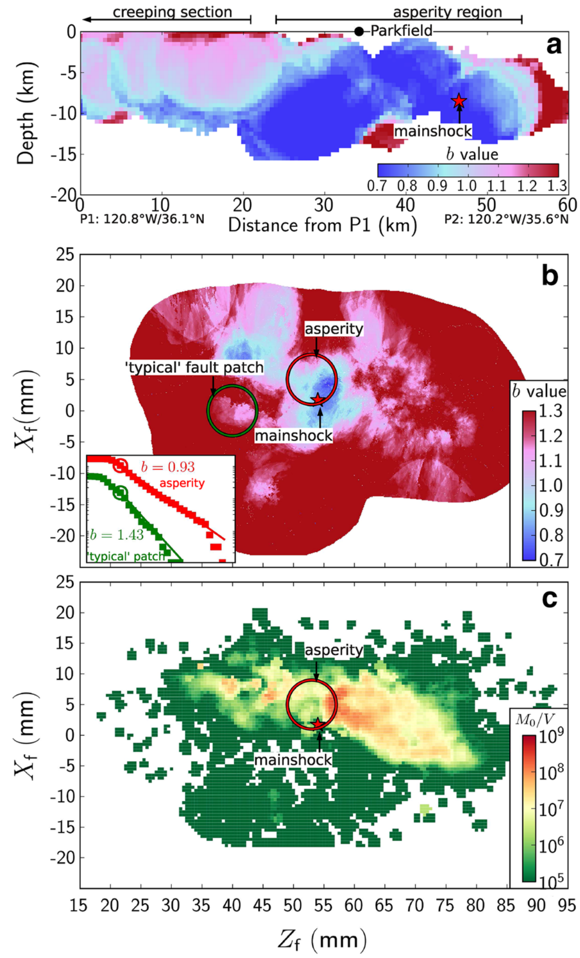

Figure 8

Comparison between b value maps at Parkfield and in the laboratory. **a** b value map of the Parkfield section of the San Andreas fault modified after Schorlemmer and Wiemer (2005). The *red star* marks the hypocenter location of the 2004, M = 6.0 mainshock. **b** Spatial b value map and frequency–magnitude distributions of an asperity region (*inset*, *red circle*) and a normal fault region (*inset*, *green circle*). **c** Map of seismic moment release per fault volume computed for events close to the fault surface (modified from Goebel *et al*. 2012)

Figure 9b shows D_H for six successive stick–slip events. The fractal dimension decreased systematically and approached a value of $D_H \approx 2$ in the interslip period before the six LSD event. Similarly, the fractal dimensions decreased with successive stick–slips during the other experiments from values between $D_H \approx 2.5$ and ~ 2.0 (Fig. 9c), highlighting a generic tendency of AEs to localize close to or within the fault zone.

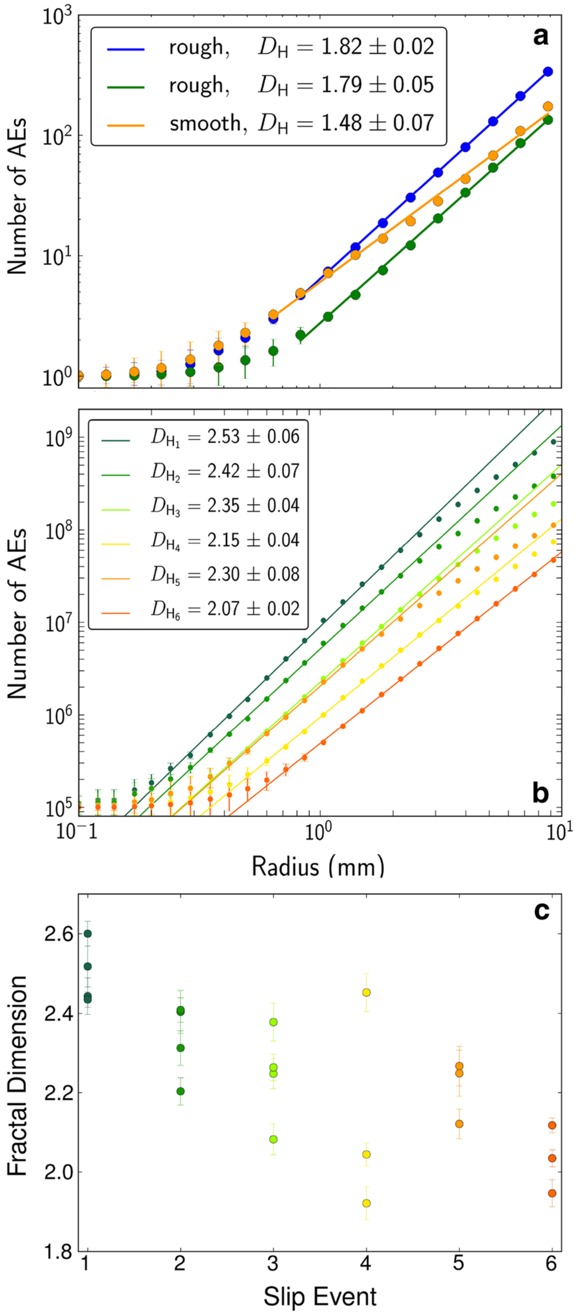

Figure 9

Changes in the AE hypocenter distributions (described here by their fractal dimension) with successive stick–slip events. **a** Fractal dimension of AEs recorded during loading of planar surfaces with pre-defined roughness. **b** Number of AE event pairs within increasing radii and corresponding fractal dimension computed from the linear part of the distributions. **c** Changes in fractal dimension with successive stick–slips. The number of markers (3 or 4) per slip event represents fractal dimensions for interslip periods of different experiments

4. Discussion

4.1. Seismic Event Statistics in Laboratory Experiments and Nature

Our experiments reveal many similarities between the distribution of AE events during laboratory stick–slip events and natural seismicity. The recorded AE populations can be described by the two fundamental relationships of statistical seismology: the Gutenberg–Richter and Omori–Utsu relationships (Omori 1894; Utsu *et al.* 1965; Ogata 1999). Spatial mapping of the seismic *b* value revealed that areas of low *b* value mark the nucleation points of stick–slip events, which is similar to the observed connection between low-*b*-value regions and mainshock locations in nature (Westerhaus *et al.* 2002; Wyss and Matsumura 2002; Schorlemmer and Wiemer 2005; Wyss and Stefansson 2006). We also illustrated that areas of low *b* values are associated with higher seismic moment release and relatively more large-magnitude AE events observed in FMDs. Larger AEs tend to cluster at relatively thin parts of the faults during periods of elevated stress before failure (Fig. 4). Thus, seismic event clustering is a result of the interaction between fault structural heterogeneity and loading stresses. More specifically, load-bearing asperities may produce clusters of relatively larger-magnitude events during the stress increase of an advancing seismic cycle. Similarly, fault asperities may be of crucial importance in the generation of areas of low *b* value in nature (Wiemer and Wyss 1997).

Besides the power-law distribution of FMDs and AE aftershocks, we showed that AE hypocenters are fractally distributed, which is also observed for natural seismicity (Aki 1981; Hirata 1989; Wyss *et al.* 2004). In the laboratory, fractal dimensions are observed to decrease rapidly before sample fracture caused by AE localization close to the point of fracture nucleation (Lei *et al.* 1992; Lockner and Byerlee 1995; Zang *et al.* 1998). Our results, on the other hand, reveal a connection between fractal dimension and fault roughness. We observed that rough, pre-cut surfaces generally produce AE hypocenter populations with larger fractal dimensions than smooth, pre-cut surfaces. Similarly, we interpret the observed decrease in D_H with successive stick–slip events on incipient fracture surfaces as an expression of progressive fault smoothing and reduction of structural complexity. This emphasizes a possible role of our experiments in guiding fractal dimension analysis for assessment of evolution of fault roughness in nature.

Our laboratory experiments revealed a general connection between fault structure and seismic event distributions suggesting that fault roughness and heterogeneity can control the spatial, temporal, and FMDs of seismicity.

4.2. Fault Structure and Slip Localization

Natural fault zones are generally complex but show distinguishable structural features, i.e. one or more fault cores, a gouge layer, zones of localized slip surrounded by a broader zone of deformed rocks (e.g. Chester *et al*. 1993; Schulz and Evans 2000; Ben-Zion and Sammis 2003; Faulkner *et al*. 2003, 2010). Within the scope of this series of experiments we showed that similar structural features can be produced after only few stick–slip events on fault zones that developed from incipient fracture surfaces. Analogous to natural faults which are surrounded by a broad zone of damage and fractures (Mitchell and Faulkner 2009; Savage and Brodsky 2011; Faulkner *et al*. 2010), we observed a wide zone of micro-cracking which extends to several millimeters in places. This zone has decreasing micro-crack and AE activity with increasing fault normal distances. Similar observations, i.e. decreasing crack densities away from the faults axis, were also made within process zones of controlled, shear-fracture experiments (Zang *et al*. 2000; Janssen *et al*. 2001). These studies highlight the importance of fracture processes during the formation of faults and secondary cracks which can exhibit their own zones of intensified mico-cracking.

Besides the direct analysis of fault structures in thin sections and CT scans, we investigated the spatial distribution of AEs and its connection with fault roughness. Systematic changes in the fractal dimension of AE events with successive stick–slip events are interpreted as being caused by fault smoothing and reduction in fault complexity. This type of fault evolution is likely to be associated with the formation of zones of slip localization, observed in post-experiment thin sections. Consequently, the deformation history of the samples during our stick–slip events includes an initial stage during which the faults are relatively rough, AE activity is high, and distributed seismic events occur. The second stage of fault formation is characterized by progressive fault smoothing and the AE hypocenters start to localize at, or within, the fault zone. During this stage, zones of localized slip form which probably accommodate most of the total displacement along the fault. We hypothesize that slip starts to localize early within thin zones of fine-grain material during our experiments. This is supported by the corresponding rapid decrease in D_H within the first three LSD events.

Localized zones of high deformation are not only limited to stick–slip experiments but are also observed after sample fracture and subsequent frictional sliding experiments (Amitrano and Schmittbuhl 2002). The authors identified localized shear bands that consist of thin layers ($\sim$0.1 mm) of elongated, smaller grains within a wider ($\sim$1 mm) gouge layer. Local shear bands in granular layers and porous rocks are likely to be transient deformation features at low strain which may mark different stages of strain localization (Aydin and Johnson 1983; Hirth and Tullis 1989; Mair *et al*. 2000). The stick–slip events during our experiments commonly produce through-going zones of strain localization and localized slip.

The structural evolution of natural fault zones may occur on very different temporal and spatial scales compared with laboratory faults. Mature fault segments are expected to show little or no structural changes after a single seismic cycle. Our laboratory faults, on the other hand, have strong structural variations, especially within the initial 1–3 stick–slip cycles (Fig. 9c). The extent of the decreases of structural variations for later stick–slips are indicative of a possible stable structural configuration of laboratory faults after many stick–slip events. The laboratory faults can thus be regarded as similar to young tectonic faults, with rapid rates of structural change. Our comparison of natural and laboratory-created faults revealed similarities of seismicity distributions despite the vastly different scales. For a more quantitative assessment of structural evolution and slip localization, more experiments with a range of strains and slip modes are required. Nevertheless, the observed structural similarities of laboratory-created and natural fault zones emphasize the importance of laboratory analog experiments for understanding fault formation. Moreover, our experiments provide insight into how complexity affects fault mechanics.

4.2.1 Subsidiary Faults and Aftershock Distributions

Part of the structural complexity of natural fault zones is generated by secondary fault structures in the vicinity of the main fault. One example of the existence of secondary fault branches is the Parkfield section of the San Andreas fault (Fig. 10b). Although the surface complexity of faults may not be identical with structural complexity at seismogenic depths, there is a connection between surface complexity and fault heterogeneity at depth, documented, for example, by variations in focal mechanisms (Bailey *et al.* 2010). Fault trace complexity also provides insight into evolutionary processes with increasing displacements (Wesnousky 1988). Analogous to natural faults, our laboratory-created fault zones are connected to secondary cracks and slip surfaces which can accommodate parts of the total displacement. The 3D representations of laboratory faults reveal the overall topography (Fig. 10e), however, the complex network of anastomosing cracks is best visualized by extracting their traces from 2D CT images (Fig. 10c, d). This representation reveals that part of the fault's topography is a result of different branches of smaller cracks with sub-parallel or low-angle orientation to the main slip surface identified by high AE activity. During our experiments, secondary structural features, for example, anastomosing crack networks, are likely to be required for creation of SSD events and aftershocks, neither of which is observed during stick–slip on simple, planar saw-cut surfaces.

Thus, our results suggest that the existence of aftershock sequences in the laboratory is linked to fault structural complexity. Similarly, aftershock sequences may be closely linked to fault complexity in nature. In nature, aftershocks are related to the slip

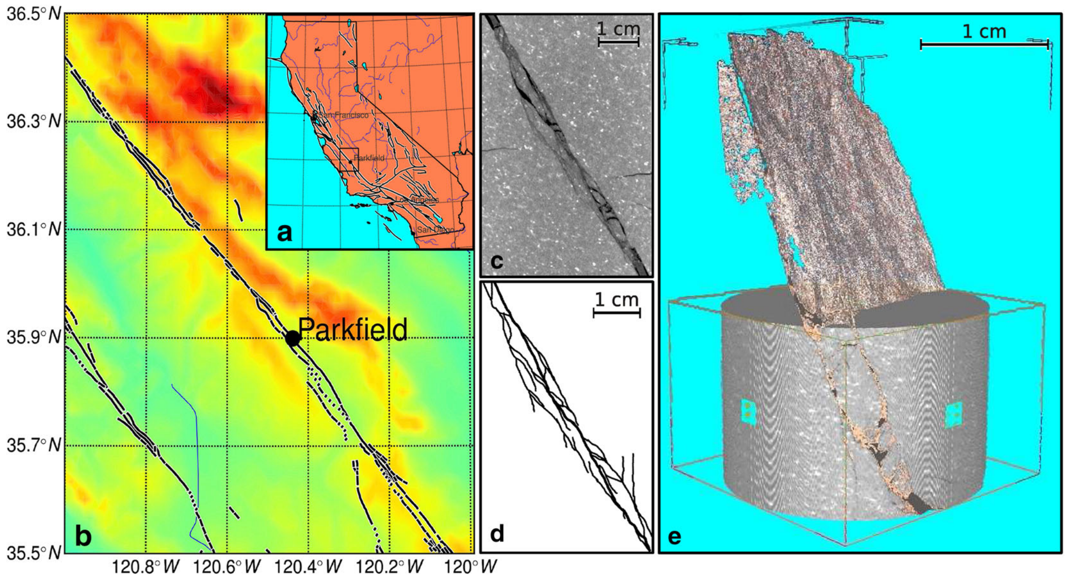

Figure 10

Traces of main faults and subsidiary faults in nature and in the laboratory. **a** Map of California with major fault traces (Californian Fault Traces 2010). The *black rectangle* marks the region plotted in **b**. **b** Fault traces including subsidiary faults close to the Parkfield section of the San Andreas fault. *Background colors* represent elevation between 100 and 1,200 m. **c** CT scan slice of the sample's center. **d** Traces of faults and secondary cracks based on the CT image in **c**. **e** 3D image of a laboratory fault revealing different fault topography and secondary cracks seen at the outer boundaries distribution during the mainshock (Wiemer and Katsumata 1999; Woessner *et al*. 2006) and to mainshock-induced changes in fault strength (Beroza and Zoback 1993) and redistribution of stress (Mendoza and Hartzell 1988). Aftershocks can also occur on secondary faults with different orientations from the principal slip surfaces (Mendoza and Hartzell 1988; Oppenheimer 1990).

5. Conclusion

We have documented the formation of laboratory fault zones from incipient fracture surfaces by means of post-experimental fault-structural analysis and by analysis of AE distributions. Our results emphasize many structural similarities between laboratory-created and natural fault zones, for example, a fault core containing a gouge layer and zones of slip localization, a damage zone with decreasing crack densities at increasing fault normal distances, and secondary, anastomosing cracks in the proximity of the main slip surface. Moreover, we observed several analogies between the statistics of AE events and natural seismicity: 1) AE events are fractally distributed in space; 2) show Omori–Utsu aftershock decay, and 3) Gutenberg–Richter frequency-magnitude distributions.

Our experiments emphasize that AE clustering in time and space is connected to fault complexity. The spatial clustering of AEs before slip events is associated with fault asperity regions. Temporal clustering, i.e. aftershock sequences, is related to the existence of fault structural complexity in stick–slip experiments.

Our results also reveal a connection between fault roughness and the fractal dimension of AE hypocenters, and suggest that changes in fault roughness as a result of successive stick–slip events can induce progressive localization of AEs. Consequently, roughness may be a controlling parameter for the spatial distribution of seismicity in the proximity of both laboratory and natural faults.

Our experiments emphasize the importance of laboratory investigations of fault complexity when assessing physical mechanisms that cause variations in micro-seismicity. Furthermore, they can advance our understanding of fault formation, and evolution with larger displacements, and the complex interplay between fault-driving stresses and fault heterogeneity before stick–slip events and earthquakes.

Acknowledgments

We thank Stefan Gehrmann and Matthias Kreplin for rock sample preparation, and Erik Rybacki for creating the CT scan images at GFZ-Potsdam, Germany. The manuscript benefitted from detailed comments by Andy Michael and an anonymous reviewer. This research was supported in part by the Southern Californian Earthquake Center under Contribution Number 11017 and 13022.

References

Aki, K. (1965), *Maximum likelihood estimate of b in the formula log $N = a - bM$ and its confidence limits*, Bull. Earthquake Res. Inst., Tokyo Univ., *43*, 237–239.

Aki, K. (1981), A probabilistic synthesis of precursory phenomena, in Earthquake Prediction: An International Review, Maurice Ewing Series, vol. *4*, edited by D. W. Simpson and P. G. Richards, pp. 566–574, American Geophysical Union, Washington, D. C.

Amitrano, D. (2003), *Brittle-ductile transition and associated seismicity: Experimental and numerical studies and relationship with the b value*, J. Geophys. Res., *108*, 2044, doi:10.1029/2001JB000680.

Amitrano, D., and J. Schmittbuhl (2002), *Fracture roughness and gouge distribution of a granite shear band*, J. Geophys. Res, *107*, 2375, doi:10.1029/2002JB001761.

Aydin, A., and A. M. Johnson (1983), *Analysis of faulting in porous sandstones*, J. Struct. Geol., *5*(1), 19–31.

Bailey, I., Y. Ben-Zion, T. W. Becker, and M. Holschneider (2010), *Quantifying focal mechanism heterogeneity for fault zones in central and southern California*, Geophys. J. Int., *83*, 433–450.

Barbot, S., N. Lapusta, and J.-P. Avouac (2012), *Under the hood of the earthquake machine: T oward predictive modeling of the seismic cycle*, Science, *336*(6082), 707–710, doi:10.1126/science.1218796.

Ben-Zion, Y., and C. G. Sammis (2003), *Characterization of F ault Z ones*, Pure Appl. Geophys., *160*, 677–715.

Bender, B. (1983), *Maximum likelihood estimation of b values for magnitude grouped data*, Bull. Seismol. Soc. Am., *73*(3), 831–851.

Beroza, G. C., and M. D. Zoback (1993), *Mechanism diversity of the Loma Prieta aftershocks and the mechanics of mainshock-aftershock interaction.*, Science, *259*(5092), 210.

Brace, W. F., and J. D. Byerlee (1966), *Stick–slip as a mechanism for earthquakes*, Science, *153*(3739), 990–992.

Byerlee, J. D. (1970), *The mechanics of stick–slip*, Tectonophys., *9*(5), 475–486.

Caine, J. S., J. P. Evans, and C. B. Forster (1996), *Fault zone architecture and permeability structure*, Geology, *24*(11), 1025–1028.

Californian Fault Traces (2010), Quaternary Fault and Fold Database for the United States, California Geological Survey & U.S. Geological Survey, http://earthquake.usgs.gov/regional/qfaults, (accessed February 17, 2012).

Chester, F. M., and J. M. Logan (1986), *Implications for mechanical properties of brittle faults from observations of the P unchbowl fault zone, California*, Pure Appl. Geophys., *124*(1), 79–106.

Chester, F. M., J. P. Evans, and R. L. Biegel (1993), *Internal structure and weakening mechanisms of the San Andreas Fault*, J. Geophys. Res., *98* (B1), 771–786, doi:10.1029/92JB01866.

Dieterich, J. (1979), *Modeling of rock friction 1. Experimental results and constitutive equations*, J. Geophys. Res., *84*(B5), 2161–2168.

Dieterich, J. H., and K. B. Richards-Dinger (2010), *Earthquake recurrence in simulated fault systems*, Seismogenesis and Earthquake Forecasting: The Frank Evison Volume *II*, 2, 233–250.

Dietrich, J. H. (1978), *Time-dependent friction and mechanics of stick–slip*, Pure Appl. Geophys., *116*, 790–806.

Dor, O., Y. Ben-Zion, T. K. Rockwell, and J. Brune (2006), *Pulverized rocks in the mojave section of the San Andreas Fault Zone*, Earth and Planetary Science Letters, *245*(3), 642–654.

Faulkner, D. R., A. C. Lewis, and E. H. Rutter (2003), *On the internal structure and mechanics of large strike-slip fault zones: Field observations of the Carboneras fault in southeastern Spain*, Tectonophysics, *367*(3), 235–251.

Faulkner, D. R., T. M. Mitchell, E. H. Rutter, and J. Cembrano (2008), *On the structure and mechanical properties of large strike-slip faults*, Geological Society, London, Special Publications, *299*(1), 139–150.

Faulkner, D. R., C. A. L. Jackson, R. J. Lunn, R. W. Schlische, Z. K. Shipton, C. A. J. Wibberley, and M. O. Withjack (2010), *A review of recent developments concerning the structure, mechanics and fluid flow properties of fault zones*, Journal of Structural Geology, *32*(11), 1557–1575, doi:10.1016/j.jsg.2010.06.009.

Faulkner, D. R., T. M. Mitchell, J. Behnsen, T. Hirose, and T. Shimamoto (2011), *Stuck in the mud? Earthquake nucleation and propagation through accretionary forearcs*, Geophys. Res. Lett., *38*(18), L18,303.

Feder, J. (1988), Fractals, Plenum Press, New York.

Goebel, T. H. W., T. W. Becker, D. Schorlemmer, S. Stanchits, C. Sammis, E. Rybacki, and G. Dresen (2012), Identifying fault hetergeneity through mapping spatial anomalies in acoustic emission statistics, J. Geophys. Res., *117*, B03310, doi:10.1029/2011JB008763.

Goebel, T. H. W., D. Schorlemmer, G. Dresen, T. W. Becker, and C. G. Sammis (2013), *Acoustic emissions document stress changes over many seismic cycles in stick–slip experiments*, Geophys. Res. Letts., 40, doi:10.1002/grl.50507.

Grassberger, P. (1983), *Generalized dimensions of strange attractors*, Physics Letters A, *97*(6), 227–230.

Green, H., and C. Marone (2002), *Instability of deformation*, Reviews in mineralogy and geochemistry, *51*(1), 181–199.

Guo, Z., and Y. Ogata (1997), *Statistical relations between the parameters of aftershocks in time, space, and magnitude*, J. Geophys. Res., *102*(B2), 2857–2873.

Gutenberg, B., and C. F. Richter (1944), *Frequency of earthquakes in California*, Bull. Seismol. Soc. Am., *34*, 185–188.

Hirata, T. (1989), *A correlation between the b value and the fractal dimension of earthquakes*, J. Geophys. Res., *94*, 7507–7514.

Hirth, G., and J. Tullis (1989), *The effects of pressure and porosity on the micromechanics of the brittle-ductile transition in Quartzite*, J. Geophy. Res., *94*(B12), 17,825–17.

Hori, T., N. Kato, K. Hirahara, T. Baba, and Y. Kaneda (2004), *A numerical simulation of earthquake cycles along the Nankai Trough in southwest Japan: lateral variation in frictional property due to the slab geometry controls the nucleation position*, Earth and Planetary Science Letters, *228*(3), 215–226.

Ishimoto, M., and K. Iida (1939), *Observations of earthquakes registered with the microseismograph constructed recently*, Bull. Earthquake Res. Inst. Tokyo Univ., *17*, 443–478.

Janssen, C., F. Wagner, A. Zang, and G. Dresen (2001), *Fracture process zone in granite: a microstructural analysis*, Int. J. Earth Sci., *90*(1), 46–59.

Lei, X., O. Nishizawa, K. Kusunose, and T. Satoh (1992), *Fractal structure of the hypocenter distributions and focal mechanism solutions of acoustic emission in two granites of different grain sizes*, J. Phys. Earth, *40*, 617–634.

Lockner, D., and J. Byerlee (1990), *An example of slip instability resulting from displacement-varying strength*, Pure Appl. Geophys., *133*(2), 269–281.

Lockner, D., J. Byerlee, V. Kuksenko, A. Ponomarev, and A. Sidorin (1991a), *Observations of quasistatic fault growth from acoustic emissions*, Fault Mech. Transport Properties of Rocks, pp. 3–31.

Lockner, D., J. Byerlee, V. Kuksenko, A. Ponomarev, and A. Sidorin (1991b), *Quasi-static, fault growth and shear fracture energy in granite*, Nature, *350*, 39–42.

Lockner, D. A., and N. M. Beeler (2002), 32 Rock failure and earthquakes, in International Handbook of Earthquake and Engineering Seismology, International Geophysics, vol. *81*, Part A, edited by P. C. J. William H.K. Lee, Hiroo Kanamori and C. Kisslinger, pp. 505–537, Academic Press, doi:10.1016/S0074-6142(02)80235-2.

Lockner, D. A., and J. D. Byerlee (1995), Precursory AE patterns leading to rock fracture, in Proc. 5th Conf. on Acoustic Emission/Microseismic Activity in Geologic Structures and Materials, pp. 45–58.

Main, I. G., P. G. Meredith, and C. Jones (1989), *A reinterpretation of the precursory seismic b-value anomaly from fracture mechanics*, Geoph. J. Int., *96*, 131–138.

Main, I. G., P. G. Meredith, and P. R. Sammonds (1992), *Temporal variations in seismic event rate and b-values from stress corrosion constitutive laws*, Tectonophysics, *211*, 233–246.

Mair, K., I. Main, and S. Elphick (2000), *Sequential growth of deformation bands in the laboratory*, J. Struct. Geol., *22*(1), 25–42.

Malin, P. E., S. N. Blakeslee, M. G. Alvarez, and A. J. Martin (1989), *Microearthquake imaging of the Parkfield asperity*, Science, *244*, 557–559.

Mandelbrot, B. (1982), The fractal geometry of nature, Freeman, New York.

Marone, C. (1998), *Laboratory-derived friction laws and their application to seismic faulting*, Annu. Rev. Earth Planet. Sci., *26*, 643–696.

Meijninger, B. M. L., and R. L. M. Vissers (2006), *Miocene extensional basin development in the Betic Cordillera, SE Spain revealed through analysis of the alhama de murcia and crevillente faults*, Basin Research, *18*(4), 547–571.

Meijninger, B. M. L., and R. L. M. Vissers (2007), *Thrust-related extension in the Prebetic (Southern Spain) and closure of the North Betic Strait*, Revista de la Sociedad Geoló gica de España, *20*(3–4), 153–171.

Mendoza, C., and S. H. Hartzell (1988), *Aftershock patterns and main shock faulting*, Bull. Seismol. Soc. Am., *78*(4), 1438–1449.

Meredith, P. G., I. G. Main, and C. Jones (1990), *Temporal variations in seismicity during quasi-static and dynamic rock failure*, Tectonophysics, *175*, 249–268.

Mitchell, T., and D. Faulkner (2009), *The nature and origin of off-fault damage surrounding strike-slip fault zones with a wide range of displacements: A field study from the Atacama fault system, northern Chile*, Journal of Structural Geology, *31*(8), 802–816, doi:10.1016/j.jsg.2009.05.002.

Mogi, K. (1962), *Magnitude-frequency relations for elastic shocks accompanying fractures of various materials and some related problems in earthquakes*, Bull. Earthquake Res. Inst. Univ. Tokyo, *40*, 831–853.

Moore, D. E., and D. A. Lockner (2004), *Crystallographic controls on the frictional behavior of dry and water-saturated sheet structure minerals*, Journal of Geophysical Research: Solid Earth, *109*(B3), doi:10.1029/2003JB002582.

Moore, D. E., and M. J. Rymer (2007), *Talc-bearing serpentinite and the creeping section of the San Andreas fault*, Nature, *448*, 795–797, doi:10.1038/nature06064.

Nadeau, R. M., and T. V. McEvilly (1999), *Fault slip rates at depth from recurrence intervals of repeating microearthquakes*, Science, *285*, 718–721.

Nadeau, W. F., R. M., and T. V. McEvilly (1995), *Clustering and periodic recurrence of microearthquakes on the San Andreas Fault at Parkfield, California*, Science, *267*, 503–507.

Narteau, C., S. Byrdina, P. Shebalin, and D. Schorlemmer (2009), *Common dependence on stress for the two fundamental laws of statistical seismology*, Nature, *462*, 642–645, doi:10.1038/nature08553.

Noda, H., and N. Lapusta (2013), *Stable creeping fault segments can become destructive as a result of dynamic weakening*, Nature, *493*(7433), 518–521.

Ogata, Y. (1999), *Seismicity analysis through point-process modeling:a review*, pageoph, *155*, 471–507.

Omori, F. (1894), *On the aftershocks of earthquake*, J. Coll. Sci. Imp. Univ. Tokyo, *7*, 111–200.

Oppenheimer, D. (1990), *Aftershock slip behavior of the 1989 Loma Prieta, California earthquake*, Geophys. Res. Lett, *17*(8), 1199–1202.

Powers, P. M., and T. H. Jordan (2010), *Distribution of seismicity across strike-slip faults in California*, J. Geophys. Res., *115*, doi:10.1029/2008JB006234.

Reasenberg, P., and L. M. Jones (1989), *Earthquake hazard after a mainshock in california*, Science, *243*(4895), 1173–1176.

Rundle, J. B., P. B. Rundle, A. Donnellan, and G. Fox (2004), *Gutenberg-richter statistics in topologically realistic system-level earthquake stress-evolution simulations*, Earth Planets and Space, *56*(8), 761–772.

Savage, H. M., and E. E. Brodsky (2011), *Collateral damage: Evolution with displacement of fracture distribution and secondary fault strands in fault damage zones*, J. Geophys. Res., *116*(B3), doi:10.1029/2010JB007665.

Scholz, C. (1998), *Earthquakes and friction laws*, Nature, *391*(6662), 37–42.

Scholz, C. H. (1968), *The frequency-magnitude relation of microfracturing in rock and its relation to earthquakes*, Bull. Seismol. Soc. Am., *58*, 399–415.

Schorlemmer, D., and S. Wiemer (2005), *Microseismicity data forecast rupture area*, Nature, *434*, 1086, doi:10.1038/4341086a.

Schorlemmer, D., S. Wiemer, and M. Wyss (2005), *Variations in earthquake-size distribution across different stress regimes*, Nature, *437*, 539–542, doi:10.1038/nature04094.

Schroeder, M. (1991), *Fractals, chaos, power laws: Minutes from an infinite paradise*, W. H. Freemann, New York.

Schulz, S. E., and J. P. Evans (2000), *Mesoscopic structure of the Punchbowl Fault, Southern California and the geologic and geophysical structure of active strike-slip faults*, J. Struct. Geol., *22*(7), 913–930.

Shcherbakov, R., D. L. Turcotte, and J. B. Rundle (2004), *A generalized omori's law for earthquake aftershock decay*, Geophys. Res. Lett., *31*, L11613, doi:10.1029/2004GL019808.

Smith, S. A. F., A. Bistacchi, T. Mitchell, S. Mittempergher, and G. Di Toro (2013), *The structure of an exhumed intraplate seismogenic fault in crystalline basement*, Tectonophysics, *599*, 29–44.

Sobiesiak, M., U. Meyer, S. Schmidt, H.-J. Gotze, and C. M. Krawczyk (2007), *Asperity generating upper crustal sources revealed by b-value and isostatic residual anomaly grids in the area of Antofagasta, Chile*, J. Geophys. Res., *112*, doi:10.1029/2006JB004796.

Stanchits, S., S. Vinciguerra, and G. Dresen (2006), *Ultrasonic velocities, acoustic emission characteristics and crack damage of basalt and granite*, Pure Appl. Geophys., *163*, 975–994.

Stesky, R. M. (1978), *Mechanisms of high temperature frictional sliding in Westerly granite*, Can. J. Earth Sci., *15*, 361–375.

Thompson, B. D., R. P. Young, and D. A. Lockner (2005), *Observations of premonitory acoustic emission and slip nucleation during a stick slip experiment in smooth faulted westerly granite*, Geophys. Res. Letts., *32*, doi:10.1029/2005GL022750.

Thompson, B. D., R. P. Young, and D. A. Lockner (2009), *Premonitory acoustic emissions and stick–slip in natural and smooth-faulted Westerly granite*, J. Geophys. Res., *114*, doi:10.1029/2008JB005753.

Utsu, T., Y. Ogata, and M. Ritsuko (1965), *The centenary of Omori formula for a decay law of afterhock activity*, Journal of Physics of the Earth, *43*, 1–33.

Voisin, C., F. Renard, and J.-R. Grasso (2007), *Long term friction: From stick–slip to stable sliding*, Geophs. Res. Lett., *34*, doi:10.1029/2007GL029715.

Ward, S. N. (2000), *San Francisco bay area earthquake simulations: A step toward a standard physical earthquake model*, Bull. Seismol. Soc. Am., *90*(2), 370–386.

Weeks, J., D. Lockner, and J. Beyerlee (1978), *Change in b-values during movement on cut surfaces in granite*, Bull. Seismol. Soc. Am., *68*, 333–341.

Wesnousky, S. G. (1988), *Seismological and structural evolution of strike-slip faults*, Nature, *335*, 340–342.

Westerhaus, M., M. Wyss, R. Yilmaz, and J. Zschau (2002), *Correlating variations of b-values and crustal deformations*

during the 1990s may have pinpointed the rupture initiation of the M_w = 7.4 zmit earthquake of 1999 August 17, Geophys. J. Int., *184*(1), 139–152.
Wibberley, C. A. J., G. Yielding, and G. Di Toro (2008), *Recent advances in the understanding of fault zone internal structure: A review*, Geological Society, London, Special Publications, *299*(1), 5–33.
Wiemer, S., and K. Katsumata (1999), *Spatial variability of seismicity parameters in aftershock zones*, J. Geophys. Res., *104*, 13,135–13,151.
Wiemer, S., and M. Wyss (1997), *Mapping the frequency-magnitude distribution in asperities: An improved technique to calculate recurrence times?*, J. Geophys. Res., *102*, 15,115–15,128.
Wiemer, S., and M. Wyss (2002), *Mapping spatial variability of the frequency-magnitude distribution of earthquakes*, Advances in geophysics, *45*, 259–V.
Woessner, J., E. Hauksson, S. Wiemer, and S. Neukomm (2004), *The 1997 Kagoshima (Japan) earthquake doublet: A quantitative analysis of aftershock rate changes*, Geophys. Res. Lett., *31*, L03605, doi:10.1029/2003GL018858.
Woessner, J., D. Schorlemmer, S. Wiemer, and P. M. Mai (2006), *Spatial correlation of aftershock locations and on-fault main shock properties*, J. Geophys. Res., *111*(B8), B08301, doi:10.1029/2005JB003961.
Wyss, M., and S. Matsumura (2002), *Most likely locations of large earthquakes in the Kanto and Tokai areas, Japan, based on the local recurrence times*, Physics of The Earth and Planetary Interiors, *131*, 173–184.
Wyss, M., and R. Stefansson (2006), *Nucleation points of recent mainshocks in southern Iceland, mapped by b-values*, Bull. Seismol. Soc. Am., *96*(2), 599–608.
Wyss, M., and S. Wiemer (2000), *Change in the probability for earthquakes in southern California due to the Landers magnitude 7.3 earthquake*, Science, *290*, 1334–1338.
Wyss, M., C. G. Sammis, R. M. Nadeau, and S. Wiemer (2004), *Fractal dimension and b-value on creeping and locked patches of the San Andreas fault near Parkfield, California*, Bull. Seismol. Soc. Am., *94*, 410–421.
Zang, A., F. Wagner, S. Stanchits, G. Dresen, R. Andresen, and M. Haidekker (1998), *Source analysis of acoustic emissions in Aue granite cores under symmetric and asymmetric compressive loads*, Geophys. J. Int., *135*, 1113–1130.
Zang, A., F. C. Wagner, S. Stanchits, C. Janssen, and G. Dresen (2000), *Fracture process zone in granite*, J. Geophys. Res, *105*(B10), 23,651–23,661.

(Received March 14, 2013, revised August 21, 2013, accepted August 23, 2013, Published online November 21, 2013)